

Scanned single-electron probe inside a silicon electronic device

Kevin S. H. Ng,^{1,2} Benoit Voisin,¹ Brett C. Johnson,³ Jeffrey C. McCallum,³ Joe Salfi,^{1,4} and Sven Rogge¹

¹*Centre for Quantum Computation and Communication Technology, School of Physics, The University of New South Wales, Sydney, New South Wales 2052, Australia*

^{2,5}*Physikalisches Institut and Center for Integrated Quantum Science and Technology, Universität Stuttgart, Pfaffenwaldring 57, 70569 Stuttgart, Germany*

³*Centre for Quantum Computation and Communication Technology, School of Physics, University of Melbourne, Melbourne, Victoria 3010, Australia*

⁴*Department of Electrical and Computer Engineering, University of British Columbia, Vancouver, BC V6T 1Z4, Canada**

Solid-state devices can be fabricated at the atomic scale, with applications ranging from classical logic to current standards and quantum technologies. While it is very desirable to probe these devices and the quantum states they host at the atomic scale, typical methods rely on long-ranged capacitive interactions, making this difficult. Here we probe a silicon electronic device at the atomic scale using a localized electronic quantum dot induced directly within the device at a desired location, using the biased tip of a low-temperature scanning tunneling microscope. We demonstrate control over short-ranged tunnel coupling interactions of the quantum dot with the device's source reservoir using sub-nm position control of the tip, and the quantum dot energy level using a voltage applied to the device's gate reservoir. Despite the ~ 1 nm proximity of the quantum dot to the metallic tip, we find the gate provides sufficient capacitance to enable a high degree of electric control. Combined with atomic scale imaging, we use the quantum dot to probe applied electric fields and charge in individual defects in the device. This capability is expected to aid in the understanding of atomic-scale devices and the quantum states realized in them.

The miniaturization of solid-state devices has driven tremendous improvements in their performance and functionality. For example, the information revolution has been enabled through decades of continuous miniaturization of silicon complementary metal-oxide-semiconductor devices. Device miniaturization also permits the localization and control of single electrons in solids, which has led to new fundamental physics experiments¹, new current standards^{2,3} and could enable the realization of quantum computers⁴⁻⁷ and quantum simulators⁸⁻¹¹. Such single electron devices can employ quantum dots (QD)¹²⁻¹⁴ or active atoms placed with atomic-scale precision in solids using scanning tunnelling microscopy (STM)¹⁴⁻¹⁸.

With ever-shrinking device sizes, real-space techniques for probing their properties and the complex states they host are becoming increasingly important. One notable technique, the scanning single electron transistor¹⁹ (SSET) monitors the capacitive response of an electron localized on scanning single-electron transistor to probe electrons in a device. Another notable technique, scanning gate microscopy (SGM)²⁰ records the electrostatic response of the device's conductance to a scanned conductive tip. The interaction mechanism at play in the SSET and SGM is capacitive (electrostatic), which inherently limits functionality and spatial resolution.

Here we go beyond the electrostatic interaction paradigm of SSET and SGM by showing that a spatially localized single-electron QD probe can be induced at an arbitrary location inside an electronic device, and made to interact not only capacitively, but also through tunneling interactions with electrons in the device. The method relies on electrostatically inducing a QD at a desired location with sub-nm precision using a biased atomically

sharp tip of a low temperature scanning tunnelling microscope (LT-STM) operating at 4.2 Kelvin²¹⁻²³. Our device consists of donor implanted source and gate reservoirs and the QD probe is induced within the device, beneath a hydrogen terminated silicon surface. This surface is atomically flat, similar to surfaces found in other materials relevant for electronic devices including two-dimensional materials^{21,22}.

Working in the regime of single-electron tunnelling through the induced QD, we demonstrate the ability to tune the tunnel coupling of the QD to the dopant-atom source reservoir by moving the STM tip, and use this to characterize the decay length of our probe QD wavefunction, which we find to be ~ 9 nm. This technique works alongside the traditional use of STM to image device surfaces with atomic resolution. Our study is performed on a multi-terminal device, having both source and gate electrodes (Figure 1a), which differs significantly from previous studies^{21,22,24,25}. We find that the QD state energy can be controlled using the device's gate voltage. The gate lever arm, which expresses the ratio of the capacitive coupling between the QD and the gate, to the total capacitance, is found to be ~ 0.08 , offering a high degree of electric control. Surprisingly, the QD capacitance is dominated by the capacitive coupling to the source terminal in the device, despite the ~ 1 nm proximity of the QD state to the metallic tip that induces it.

The QD state energy also reacts to atomic scale defects that we directly observe with atomic resolution, allowing us to map the defect charge state directly using the QD. Extended to devices based on arrays of dopant atoms placed with atomic precision, we envision these new experimental capabilities could be used to character-

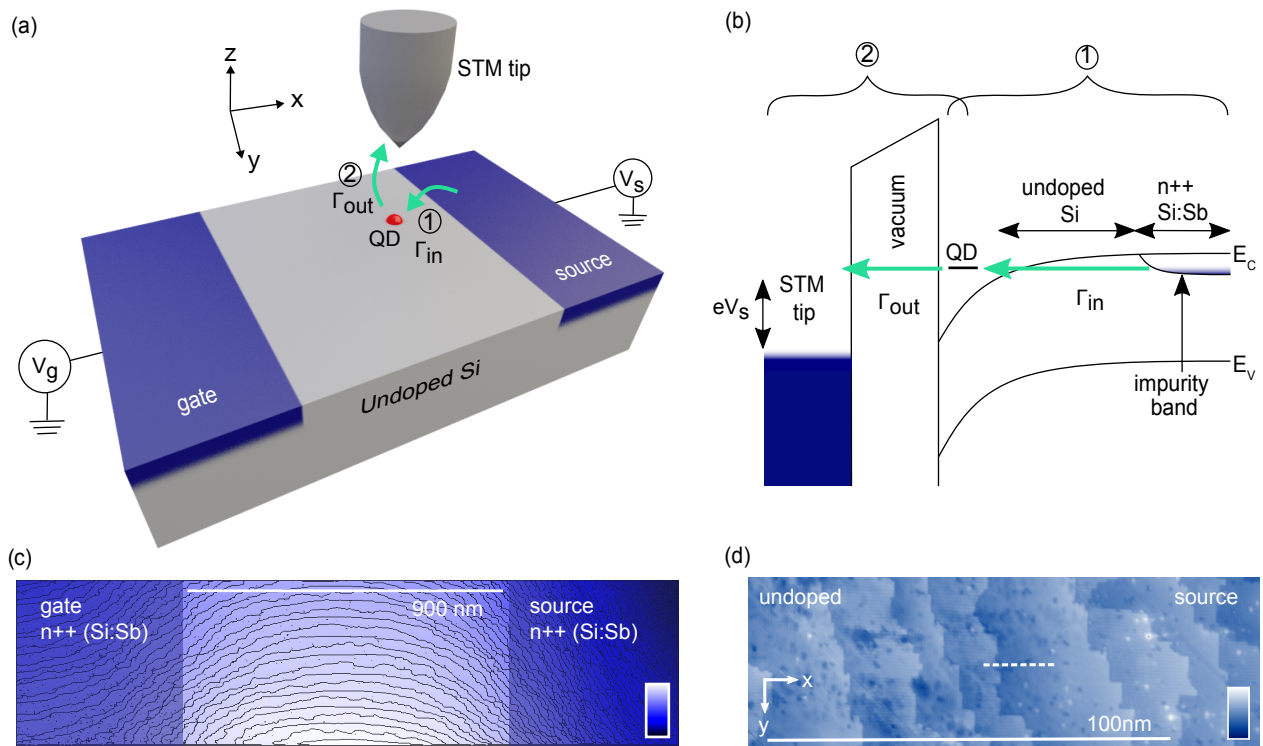


FIG. 1. Induced QD probe. (a) Experimental schematic of the device, where single electron tunnelling occurs from a biased antimony donor (source) reservoir to the QD and out to the tip. By moving the tip closer to the source reservoir, the tunnel coupling between QD and reservoir is controllably increased. Opposite the source reservoir, an additional antimony reservoir is biased to provide a gate voltage, influencing the energy of the QD. (b) Energy band diagram during resonant electron tunnelling. Single electrons tunnel through a state of the QD created by tip-induced band bending from an applied bias V_s . E_C and E_V are the conduction and valence band edges, respectively. (c) Global topography of the device (nominal shown). Step edges, identified by an edge finding algorithm and superimposed on the data, are found to be bunched in the vicinity of the gate/undoped and undoped/source junctions. Scale: 0 – 7.2 nm. (d) STM image of the sample surface at the undoped-source junction taken at $V_s = -1.6$ V. The junction is identified by a change in the appearance of the dangling bonds. The line indicates the position where the QD measurements presented in Figure 2 are performed. Scale: 0 – 0.66 nm.

ize or enhance the functionality of atomic scale devices. For example, the induced QD could be used to induce a highly tunable super-exchange²⁶ between donor atoms²⁷, or to implement local spin readout²⁸ on atomic structures consisting of interacting dopant atoms forming quantum simulators¹⁰.

Before discussing our experiment, we first describe the concept of our induced QD probe. When a negative sample bias V_s is applied to a semiconductor with respect to an STM tip, an electric field is induced by the tip that locally bends the semiconductor bands downward to create an attractive potential for electrons. We use this capability to trap individual electrons beneath our atomically flat surface²³. This is done in the insulating p-type region of a device, fabricated as a planar $n^{++}/p/n^{++}$ junction over a p-type substrate (see supp. mat.), where the antimony doped n^{++} regions form electron reservoirs that act as a source and gate (Figure 1a,c). Since the electric field is strongest below the tip, the QD follows the position of the tip, and in our experiment, we move the QD toward the source reservoir, performing resonant

single-electron tunnelling spectroscopy on the QD. Resonant tunnelling (Figure 1b) is detected as a measured step (peak) in current (conductance) when the QD state is on resonance with the source reservoir. We control the electron tunnel-in rate Γ_{in} from the source reservoir to the QD using the sub-nanometre positioning precision of the STM tip along x and z (Figure 1a) and track the variation of Γ_{in} through the measured single-electron tunnelling current $I = e(\Gamma_{in}^{-1} + \Gamma_{out}^{-1})^{-1}$, where Γ_{out} is the tunnel rate from the QD out to the tip²⁹ and e is the electronic charge. To observe the variation of Γ_{in} , we work in the regime where $\Gamma_{in} \ll \Gamma_{out}$, which can be achieved by varying Γ_{out} using the tip-sample separation (vacuum barrier width). A voltage V_g is applied to the gate reservoir located approximately 900 nm away from the source reservoir, which we use to tune the energy of the QD. As expected for a single-electron device, this changes the corresponding bias V_s at which a QD state is on resonance with the source reservoir.

Following fabrication of the device (Figure 1a and supp. mat.), we first imaged the device at the level of

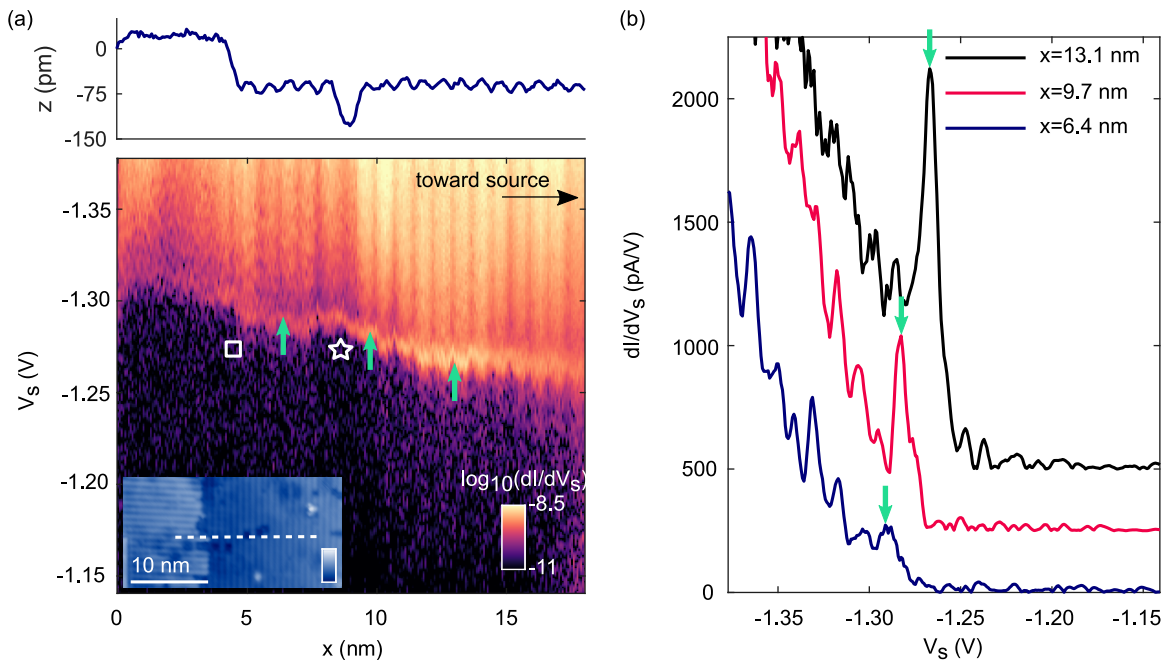


FIG. 2. Spatially resolved resonant single electron tunnelling through the QD. (a) Conductance map taken over an 18 nm distance at the line and the corresponding surface topography (top). A spatially continuous peak in conductance is observed as the tip is moved toward the reservoir, indicative of single electron tunnelling through a tip induced QD. The positions of the square and star correspond to a terrace step edge and dimer vacancy respectively the QD encountered during measurement. The position of the arrows on the resonance correspond to the traces shown in (b). Taken at $V_g = -1.6$ V. Inset: zoomed-in topography image showing the same line as Figure 1d, taken at $V_s = -1.6$ V. Scale: 0 – 0.38 nm. (b) Single conductance traces of the conductance map taken at equal intervals along the resonance. Traces are offset by 250 pA/V for clarity. The height of the single resonance peak indicated by the arrows increases as the tip approaches the reservoir.

its global topographical features, and then in detail at the junction between the undoped region and the source region (Figure 1c,d). The device is identified by the bunching of step edges at both the gate/undoped and undoped/source junctions (Figure 1c). The distinct difference in appearance of dangling bonds in the doped and undoped regions confirms that the step-edge bunching occurs at the junction (Figure 1d). Dangling bonds appear ‘bright’ (negatively charged) in doped regions and ‘dark’ (positively charged) in undoped regions in filled state imaging³⁰. Spatially resolved spectroscopy was performed at several lines traversing the junction, such as the one in Figure 1d.

The differential conductance dI/dV_s , obtained by numerically differentiating the current I , is shown as a function of source-tip bias V_s and tip position x in Figure 2a for the line shown in the STM inset. The corresponding topography z recorded by the tip is plotted above the conductance map. From $x = 0 - 4$ nm, no clear resonance is seen as tunnelling to any localized state below the tip is prevented by the wide substrate tunnel barrier. As the tip moves closer to the source reservoir, the resonance peak becomes apparent for $x \gtrsim 4$ nm at a voltage $V_s \approx -1.3$ V, and remains visible for increasing x . We also note a weak background corresponding to direct tunnelling from the occupied valence band to the tip energy

starting around $V_s \approx -1.1$ V to -1.2 V, as expected near an n-type lead³¹. Importantly, only the feature emerging at $V_s \approx -1.3$ V has a resonant peak lineshape indicative of a QD state. We plot in Figure 2b the numerically differentiated conductance for traces of Figure 2a at the coordinates $x = 6.4$ nm, $x = 9.7$ nm and $x = 13.1$ nm.

The combination of the resonance lineshape, its continuous spatial nature, and its increasing amplitude with decreasing distance from the reservoir allows us to confidently rule out that the resonance is due to tunnelling through stray dopants at the junction or surface dangling bonds^{30–32}. The possibility that the peak emerging at $x \approx 4$ nm consists of a QD state hybridized with dopants or dangling bonds can also be ruled out, because we do not observe the spectroscopic signature of dopants³¹ and dangling bonds³² in Figure 2a. For $x \gtrsim 13$ nm however, we note the conductance of the resonance levels off and even slightly decreases. It is difficult to isolate the reason for this decrease but we note that it coincides with the QD reaching localized states³¹ observed in our measured spectra (supp. mat. Figure 6). Indeed, fixed localized states in the sample are expected to be found when the tip enters the reservoir region for $x \gtrsim 18$ nm, since the reservoir is composed of antimony donor levels that are energetically below the induced QD resonance. Tunnelling here is expected to be more complex because

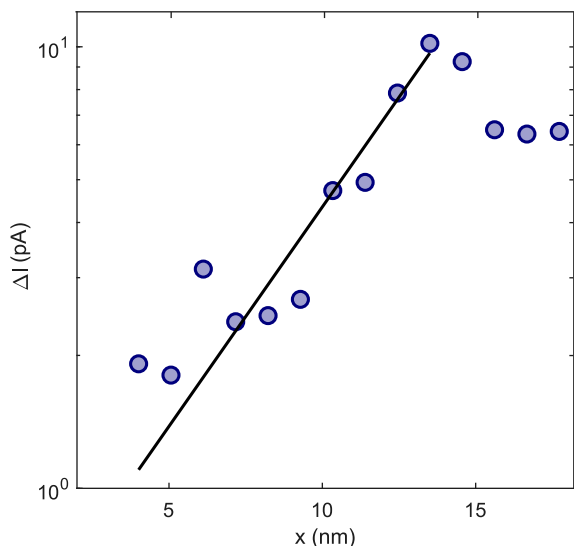


FIG. 3. Probing the QD wavefunction in space. Change in the induced current during resonant tunnelling as a function of tip position. Prior to the localized states beyond $x = 13$ nm, the increase in the current between $x = 4.0 - 13$ nm due to QD-reservoir wavefunction overlap increases exponentially, where $\kappa = 0.23 \pm 0.06 \text{ nm}^{-1}$ for a fit $\Delta I \propto \exp(\kappa x)$. This gives an estimate of the QD wavefunction decay length λ to be around 9 nm.

of the potential hybridization of the induced QD with donors²³ which have a high concentration in the reservoir.

The QD energy and tunnelling rate to the QD are expected to be influenced when the QD encounters and interacts with surface defects. This is seen in Figure 2a as two disturbances of the resonance energy in V_s , indicated by the square and star that occur at positions where a step-edge and atomic defect are found on the surface, respectively. In measurements performed along a different line towards the reservoir (supp. mat. Figure 5), we observe strong disturbances of the tunnelling current as the QD encounters accumulated negative charge at a step edge, and from a negatively charged ($2e^-$) dangling bond, at $x = 24$ nm and 32 nm respectively. For both disturbances, the bias V_s required to maintain resonant tunnelling through the QD decreases (more negative) as it moves toward the negative charge, before subsequently increasing as it moves away. This is expected, because the induced QD energy level is sensitive to surface charge in the device through the Coulomb interaction.

We now investigate the interaction of the induced QD with the planar electric field established between the biased source and gate reservoirs. In Figure 2a, the voltage V_s required to bring the QD on resonance with the source reservoir increases from -1.3 V to -1.27 V over a 9.2 nm distance between $x = 4.0 - 13.2$ nm as the QD approaches the reservoir. This is expected because of the x oriented electric field E_x that exists between the source V_s and the fixed gate $V_g = -1.6$ V during spectroscopy, which

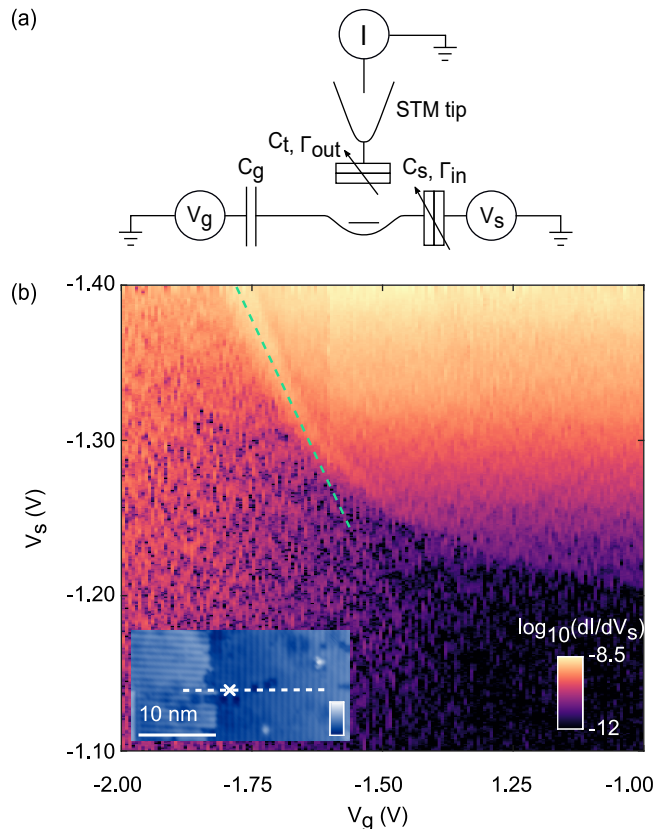


FIG. 4. Tuning the QD energy level with the gate. (a) Circuit schematic of the device. The gate voltage V_g is swept with the tip held at the position of the marker in the STM inset of (b). C_t , C_s and C_g are the capacitance between the QD and tip, source and gate respectively. (b) Charge stability diagram showing the ability to influence the energy of the QD state with a gate. The resonance follows the green line for values less than $V_g = -1.6$ V, indicating a constant capacitive coupling between the QD and its environment in this voltage range. The non-linear, weaker behaviour of the gate for values greater than -1.6 V can be explained by an increase in the stray capacitance experienced by the QD near the source due to the increasingly attractive gate potential. Inset: zoomed-in topography image showing the same line as Figure 1d, where the marker on the line indicates the position of the tip during measurement. Taken at $V_s = -1.6$ V. Scale: 0 – 0.38 nm.

introduces an x -dependent offset to the QD energy. Assuming a resonance around $V_s = -1.3$ V, a gate voltage $V_g = -1.6$ V, and a source to gate distance of approximately 900 nm, we estimate $E_x \approx 0.4$ MV/m, varying slightly for $V_s = -1.3$ V to $V_s = -1.27$ V where the resonance is found. Since the gate voltage V_g is always more negative compared to V_s during measurements, the electric potential is more repulsive when the QD is closer to the gate reservoir. As a result, when the QD moves away from the gate i.e. tip position x increases, less tip-induced band bending and a higher V_s is required to bring the QD state on resonance with the source reservoir. From E_x , we quantify the ability of the sample-tip bias voltage

to change the energy of the QD state ΔE with the lever arm parameter α_0 , where $\Delta E = e\alpha_0(V_{s,2} - V_{s,1})$ and $V_{s,1}$, $V_{s,2}$ are differing values of source-tip bias. By equating the energetic change of the resonance in Figure 2a toward lower values as x increases, to the expected energy level change due to E_x , we obtain a value of $\alpha_0 \approx 0.1$. This is in good agreement with values of α_0 independently obtained by fitting to a model of single electron tunnelling between Fermi reservoirs through a quantized state³³, and in agreement with previously extracted values of the lever arm for a tip-induced QD²³. Using this model, where fitting is facilitated by increased smoothing of the measured current, we find α_0 varying from ≈ 0.14 to 0.08 for x increasing between 11.8 – 17.8 nm, as the induced QD approaches the reservoir. For the two different intervals in x which only have approximately 1 nm overlap, the estimated values for α match closely, giving us confidence in the obtained values. We note that varying V_s and x could also change the QD potential and its energy spectrum²¹, however, the behaviour of the ground state seems to follow a relatively simple model with an energy shift of the level due to the x oriented electric field.

We estimate the decay of the tail of the induced QD wavefunction in space using the measured change in induced current $\Delta I(x)$ through the QD as it is moved toward the source reservoir with increasing x . We plot in Figure 3 $\Delta I(x)$ using the measured current of Figure 6 (supp. mat.) before the QD encounters the localized states. The blue dots plotted on the resonance of the conductance map indicate the position of the traces in x and the peaks in V_s used. For 14 traces along the resonance, we find $\Delta I(x)$ exponentially increasing between $x = 4.0 - 13$ nm before slightly decreasing ≈ 5 nm prior to encountering the localized states. This observation suggests that the appearance of the resonance at $x \approx 4$ nm is due to the increasing tunnel coupling $\Gamma_{in}(x)$ as the QD moves towards the source reservoir. Indeed, we work at a tip-sample separation that establishes a tunnel rate where $\Gamma_{out}(z)$ is larger than the tunnel rate from source reservoir to the QD $\Gamma_{in}(x)$, which depends on the QD-reservoir distance. This regime can be achieved by starting sufficiently far away from the reservoir such that Γ_{in} is much smaller than our measurement resolution of around 50 fA. Notably, we verified this regime of operation by tip-height dependent measurements closer to the reservoir (supp. mat. Figure 7).

Between $x = 4.0 - 13$ nm where we measure resonant tunnelling only between the reservoir and the QD, we obtain a best fit value for $\Delta I(x) \propto \exp(\kappa x)$ of $\kappa = 0.2288 \text{ nm}^{-1}$ (Figure 3, black line). To relate this to the decay of the induced QD wavefunction in space, we compare the decay to a model for the tunnel coupling $t = \langle \psi_{QD} | V_{QD} | \psi_{res} \rangle$ from the source reservoir to the QD that approximates the tail of the QD wavefunction as $\psi_{QD} \approx A \exp(-|x|/\lambda)$, where λ is the decay length. With an abrupt model for the reservoir electrons ψ_{res} (supp. mat.), we obtain $I \propto t^2 \propto \exp(-2|x_0|/\lambda)$, where x_0 is the

position of the reservoir relative to the QD, and from this $\lambda = 2/\kappa \approx 9$ nm using the extracted κ . We note that our assumption of an abrupt reservoir makes this an upper bound on the actual decay. Notably, the slowly varying tail is convenient to controllably tunnel couple the QD to elements such as individual donors in devices. For example, highly tunable tunnel coupling would be advantageous for local spin readout on small scale dopant-based quantum simulators^{10,34,35} where STM tips can be positioned with sub-nanometre accuracy.

By sweeping the gate voltage V_g applied to the gate donor reservoir, we demonstrate the ability to electrically tune the energy of the QD at a fixed tip-sample voltage using the gate. Figure 4a shows a schematic of our device: capacitive interactions between the QD and the tip, source and gate reservoirs are represented by C_t , C_s and C_g respectively, and are present as we keep the tip fixed in space whilst varying V_g . We vary the gate voltage V_g over a 1 V range from -2 V to -1 V to examine the gating characteristics of the QD, with the tip held at the position indicated by the marker on the line in the STM inset of Figure 4b. Figure 4b shows the conductance through the QD as a function of V_s and V_g . The green line indicates linear behaviour of the gate during resonance for $V_g \lesssim -1.6$ V. When V_g is increased toward -1 V, higher values of V_s are required to keep the QD state on resonance with the source reservoir. As expected, a more positive gate with an increasingly attractive potential pulls the level of the QD lower in energy. Thus, V_s increases and the amount of tip-induced band bending required is lessened, with a corresponding decrease in current through the QD as a consequence of the widening tunnel barrier.

We analyze the capacitive coupling of the quantum dot, and extract the gate lever arm α_g in the voltage range $V_g = -1.8$ to -1.6 V where the gate acts linearly. Here, the change in bias voltage required to maintain resonant tunnelling is given by $\partial V_s / \partial V_g = C_g / (C_\Sigma - C_s)$, where C_Σ is the sum of all capacitances between the QD and its environment, including a stray capacitance not shown in Figure. 4a. In this regime, $\partial V_s / \partial V_g \sim 0.77$ is extracted from the gradient of the green line. Using the lever arm extracted from the source bias dependent measurement, where $\alpha_0 = (C_\Sigma - C_s) / C_\Sigma \sim 0.1$ (supp. mat.), we find that $C_s / C_\Sigma \sim 0.9$ and obtain a gate lever arm for the induced quantum dot of $\alpha_g \equiv C_g / C_\Sigma \sim 0.08$. Evidently, the QD capacitive coupling is dominated by C_s , with an appreciable gate capacitive coupling, where $C_g / C_t \sim 3.4$ (supp. mat.) despite the metal tip being only ~ 1 nm away from the QD. The effect of the gate weakens for values $V_g = -1.5$ V and higher and V_s flattens out around ~ -1.215 V. This behaviour could be due to an enhancement of stray capacitance due to an accumulation of charges in or near the source, by the gate. The control of the induced QD by the gate is important for the potential use of the QD to understand the operation of devices or to probe quantum states induced in devices.

In conclusion, we have demonstrated the ability to induce a single localized electron QD within a device, and to tune its tunnel coupling to a source electrode and electric interaction with a gate electrode within a silicon electronic device. We find that the single electron QD reacts to charges present in the device, both due to individual defects, and due to voltages applied to gates in the device. With the sub-nanometre precision of the tip and the slowly-varying nature of the ground state QD wavefunction, a high level of tunnel coupling control to donor-based electrodes is possible. This opens up the possibility to use tip-induced quantum dots to characterize devices and the quantum states they host, and even to add new device functionality. We expect this technique will be applicable to advanced devices based on materials that can be engineered at the atomic scale, because it is compatible with LT-STM, the most common technique for probing atomic-scale materials and assembling atomic-scale devices^{16,17}.

ACKNOWLEDGEMENTS

K.S.H.N. would like to acknowledge S. Loth for useful discussions. We acknowledge support from the ARC Centre of Excellence for Quantum Computation and Communication Technology (CE170100012) and an ARC Discovery Project (DP180102620). J.S. acknowledges financial support from an ARC DECRA fellowship (DE1601101490) and from the National Science and Engineering Research Council. B.C.J. and J.C.MC acknowledge the AFAiR node of the NCRIS Heavy Ion Capability for access to ion-implantation facilities.

AUTHOR CONTRIBUTIONS

J.S. proposed the idea to probe an electronic device using an induced quantum dot, with input from B.V. and S.R. S.R. proposed the in-situ devices scheme with input from B.V. and J.S. K.S.H.N. performed all the measurements and analysis with input from J.S., B.V. and S.R. B.V., B.C.J. and J.C.MC. led the design, fabrication, vacuum preparation and measurement scheme for in-situ use of the device with input from J.S. and S.R. K.S.H.N. wrote the manuscript with guidance from J.S. and input from B.V. and S.R.

SUPPLEMENTARY INFORMATION

A. Device Fabrication

All measurements are performed using an Omicron LT STM at 4.2 K. A commercial p-type boron doped silicon wafer is used with a doping density of $\approx 10^{15-16} \text{ cm}^{-3}$, corresponding to a resistivity of $\approx 1-10 \text{ } \Omega \cdot \text{cm}$. Antimony ion beam implantation is performed such that a dopant layer is created just below the silicon surface with a density of $\approx 1 \times 10^{15} \text{ cm}^{-2}$ at selected regions of the sample with the use of a 120 nm thick HSQ oxide mask. Once cleaned, the sample is degassed at 600 °C for 12 hours. Following this, two additional flashes at $\approx 1000 \text{ } ^\circ\text{C}$ are performed, each for 10 seconds. The temperature is then rapidly brought to 800 °C before slowly decreasing the temperature at a rate of 10 °C/second to 340 °C to allow for the silicon surface reconstruction. Hydrogen passivation is then performed at 340 °C for approximately 6 minutes at a pressure of $6 \times 10^{-7} \text{ mbar}$ before transferring the sample to the STM for measurements with a base temperature of $2 \times 10^{-11} \text{ mbar}$.

B. Additional resonance and gating characteristics

Additional spectroscopy measurements discussed in the main text are presented in Figure 5 and 6.

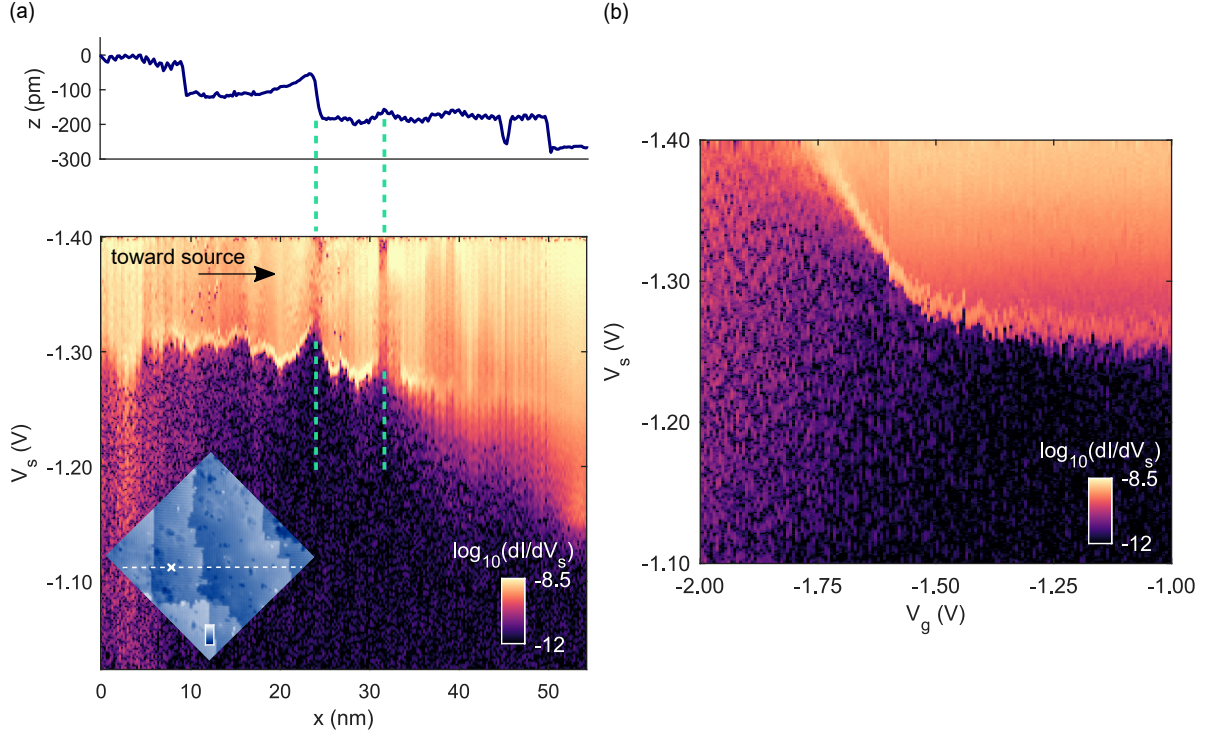


FIG. 5. (a) Spectroscopy measurements along a line at a different position in y traversing the same undoped-source junction, 58 nm away from the measurements of Figure 2a. A resonance is again observed with characteristics of the same tip-induced QD in Figure 2a. As the QD travels along the line indicated in the STM image inset, the tunnelling resonance is disturbed by the QD encountering a step edge and a dangling bond indicated by the green dashed lines at $x = 24$ nm and 32 nm respectively. From the topography above, the tip moves up 60 pm in z as it approaches the step edge of the terrace between $x = 10 - 23$ nm, likely due to accumulated negative charge at the step edge. At $x = 32$ nm, the small rise in topography reflects the tip passing over the edge of a negatively charged ($2e^-$) dangling bond, where a bright ring surrounds the characteristic halo³⁰ of a dangling bond that is momentarily positive when imaged by the tip in an un/weakly doped sample. Both sources of localized charge increase the QD energy before disturbing resonant tunnelling, as expected for a repulsive interaction. As the tip continues to approach the reservoir, the resonance is eventually not visible, indicating that the QD has been fully driven in to a region of the reservoir with a high donor density. Resonant tunnelling is no longer observed and the tip then probes the filled state density of the donor reservoir. Taken at $V_g = -1.6$ V. Inset: topography image taken at $V_s = -1.6$ V. Scale: 0 – 0.36 nm. (b) Gating characteristics of the resonance taken at the position indicated by the marker on the line of the inset in (a). The same gating behaviour is seen for the QD when compared to Figure 4b.

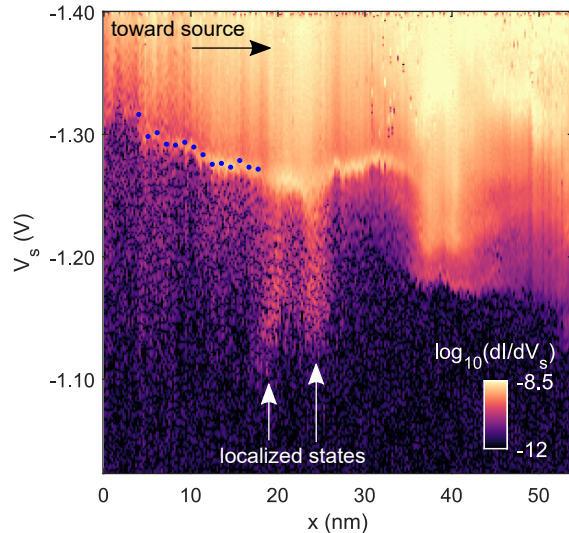


FIG. 6. A separate and extended spectroscopy measurement along the same line used for the measurements of Figure 2. The QD is driven deep in to the donor reservoir, indicated by the resonance not observed for $x \gtrsim 35$ nm. By moving the tip and QD beyond $x = 18$ nm, we observe the QD interacting with localized states around $x \approx 17 - 25$ nm and also at $x \approx 35 - 50$ nm for voltages between -1.25 V to -1.12 V, which requires less tip-induced band-bending compared to the QD state. The blue dots plotted on the resonance show the conductance peak positions used to calculate $\Delta I(x)$. Taken at $V_g = -1.6$ V.

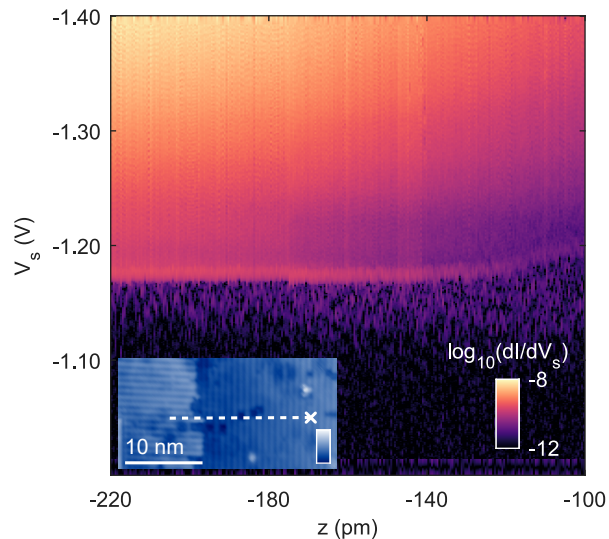


FIG. 7. Conductance map during resonant tunnelling as a function of tip height z , with the tip placed at the position of the marker on the line of the STM inset ($x = 18$ nm). Despite the slight reduction in conductance for $x \gtrsim 13$ nm, Γ_{in} here at $x = 18$ nm is larger than its corresponding value when the resonance is first observed at $x \approx 4$ nm. At this point where the tip is closest to the reservoir (for Figure 2), no significant change in the conductance peak height and lineshape is observed ± 20 pm from $z = -200$ pm, the tip height setpoint used for the measurement of Figure 2. Thus, the tunnelling regime $\Gamma_{\text{in}} \ll \Gamma_{\text{out}}$ is established during resonant tunnelling. Done when $V_g = -1.4$ V, a 0.2 V difference in V_g is not expected to result in any change in the tunnelling regime. As z is increased, the resonance weakens and is eventually not visible as expected. Inset scale: 0 – 0.38 nm.

C. Calculation of t dependence on ψ_{QD}

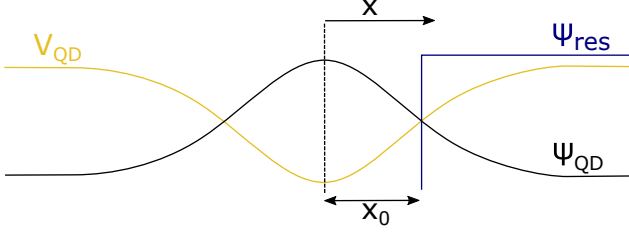


FIG. 8. Simplified schematic model of reservoir/QD wave-function overlap.

Assuming the QD potential V_{QD} is parabolic around the tip (\sim QD centre)²¹ while slowly varying in x and y to 0 far away from the tip, we approximate the tail of ψ_{QD} with an exponentially decaying function $\psi_{QD} = A \exp(-|x|/\lambda)$ and assume the donor reservoir ψ_{res} as homogeneous, normalized to 1 for $x > x_0$, the distance between QD centre and reservoir edge, and 0 otherwise. This is schematically illustrated in Figure 8.

$$\begin{aligned}
 t &= \langle \psi_{QD} | V_{QD} | \psi_{res} \rangle \\
 &= AV_{QD} \int_{-\infty}^{\infty} \exp(-|x|/\lambda) \psi_{res} dx \\
 &= AV_{QD} \int_{x_0}^{\infty} \exp(-|x|/\lambda) dx \\
 &= -AV_{QD} \lambda [\exp(-|x|/\lambda)]_{x_0}^{\infty} \\
 &= AV_{QD} \lambda \exp(-|x_0|/\lambda)
 \end{aligned}$$

$I \sim t^2 \sim \exp(-2|x_0|/\lambda)$ as $\exp(-2|x_0|/\lambda)$ is faster than λ^2 . So as the QD approaches the reservoir i.e. x increases, x_0 decreases and the current I increases exponentially as measured.

D. Calculation of the gate lever arm and additional capacitance ratios

$$\frac{C_S}{C_T} = \frac{C_S}{C_G} \frac{C_G}{C_T} \approx 39$$

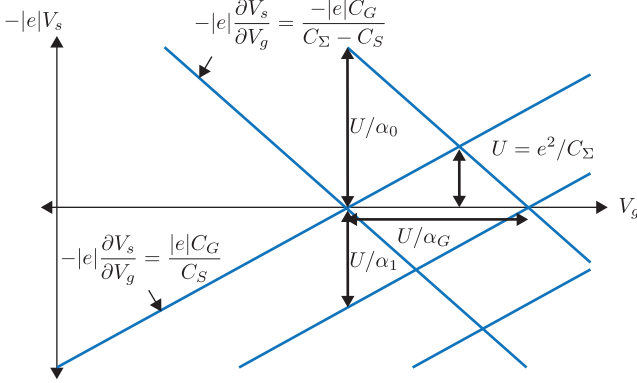


FIG. 9. Stability diagram of a single-electron transistor. One of the measured slopes and a measured lever arm parameter are used together to deduce the gate lever arm α_G , which could not be deduced directly from our experiment.

The two measured quantities $\partial V_s/\partial V_g$ and the bias lever arm α_0 can be deduced using only slopes from the Coulomb diagram pattern of the orthodox model for single-electron tunneling. This model is defined in terms of the source capacitance C_S , the gate capacitance C_G , the tip capacitance C_T , and a stray capacitance C_0 (see Fig. 4a), and the total QD self-capacitance $C_\Sigma = C_S + C_G + C_T + C_0$, and the stability diagram is shown in Fig. 9 from reference 13.

First, from Fig. 9 we can deduce that for $V_s < 0$, the measured parameter $\partial V_s/\partial V_g$ corresponds to $C_G/(C_\Sigma - C_S)$, which was experimentally determined to be 0.77. Second, from Fig. 9 we can also deduce that $\alpha_0 = (C_\Sigma - C_S)/C_\Sigma$, which was experimentally determined to be $\alpha_0 \approx 0.1$, and $\alpha_1 = C_S/C_\Sigma$. We can re-write the definition of the gate lever arm $\alpha_G \equiv C_G/C_\Sigma$ in terms of measured quantities α_0 and $\partial V_s/\partial V_g$ as follows:

$$\alpha_G \equiv \frac{C_G}{C_\Sigma} = \frac{C_G}{C_\Sigma - C_S} \frac{C_\Sigma - C_S}{C_\Sigma}$$

which is equivalent to $\alpha_g = \alpha_0 \partial V_s/\partial V_g \approx 0.1 \times 0.77 \approx 0.08$ as discussed in the main text.

Additional capacitance ratios comparing the coupling between the QD and source, gate and tip are calculated (assuming negligible stray capacitance C_0) as follows:

$$\frac{C_G}{C_T} = \frac{C_G/(C_G + C_T)}{1 - C_G/(C_G + C_T)} = \frac{0.77}{1 - 0.77} \approx 3.4$$

$$\frac{C_S}{C_G} = \frac{1 - \alpha_0}{\alpha_0 C_G/(C_G + C_T)} = \frac{1 - 0.1}{0.1 \times 0.77} \approx 12$$

- * jsalfi@ece.ubc.ca
- ¹ Goldhaber-Gordon, D. *et al.* Kondo effect in a single-electron transistor. *Nature* **391**, 156–159 (1998). URL <https://doi.org/10.1038/34373>.
 - ² Pekola, J. P. *et al.* Single-electron current sources: Toward a refined definition of the ampere. *Reviews of Modern Physics* **85**, 1421–1472 (2013). URL <https://link.aps.org/doi/10.1103/RevModPhys.85.1421>.
 - ³ Rossi, A. *et al.* An accurate single-electron pump based on a highly tunable silicon quantum dot. *Nano Letters* **14**, 3405–3411 (2014). URL <https://doi.org/10.1021/nl500927q>.
 - ⁴ Loss, D. & DiVincenzo, D. P. Quantum computation with quantum dots. *Physical Review A* **57**, 120–126 (1998). URL <https://link.aps.org/doi/10.1103/PhysRevA.57.120>.
 - ⁵ Kane, B. E. A silicon-based nuclear spin quantum computer. *Nature* **393**, 133–137 (1998). URL <http://dx.doi.org/10.1038/30156>.
 - ⁶ Petta, J. R. *et al.* Coherent Manipulation of Coupled Electron Spins in Semiconductor Quantum Dots. *Science* **309**, 2180–2184 (2005).
 - ⁷ Koppens, F. H. L. *et al.* Driven coherent oscillations of a single electron spin in a quantum dot. *Nature* **442**, 766–771 (2006).
 - ⁸ Feynman, R. P. Simulating physics with computers. *International Journal of Theoretical Physics* **21**, 467–488 (1982). URL <http://dx.doi.org/10.1007/BF02650179><http://link.springer.com/article/10.1007%2FBF02650179>.
 - ⁹ Singha, A. *et al.* Two-Dimensional Mott-Hubbard Electrons in an Artificial Honeycomb Lattice. *Science* **332**, 1176–1179 (2011).
 - ¹⁰ Salfi, J. *et al.* Quantum simulation of the hubbard model with dopant atoms in silicon. *Nat Commun* **7**, 11342 (2016). URL <https://www.ncbi.nlm.nih.gov/pubmed/27094205>.
 - ¹¹ Hensgens, T. *et al.* Quantum simulation of a fermiãŠhubbard model using a semiconductor quantum dot array. *Nature* **548**, 70 (2017). URL <http://dx.doi.org/10.1038/nature23022>.
 - ¹² Kouwenhoven, L. P., Austing, D. G. & Tarucha, S. Few-electron quantum dots. *Reports on Progress in Physics* **64**, 701 (2001). URL <http://stacks.iop.org/0034-4885/64/i=6/a=201>.
 - ¹³ Hanson, R., Kouwenhoven, L. P., Petta, J. R., Tarucha, S. & Vandersypen, L. M. K. Spins in few-electron quantum dots. *Reviews of Modern Physics* **79**, 1217–1265 (2007).
 - ¹⁴ Zwanenburg, F. A. *et al.* Silicon quantum electronics. *Reviews of Modern Physics* **85**, 961–1019 (2013).
 - ¹⁵ Fuechsle, M. *et al.* A single-atom transistor. *Nat Nanotechnol* **7**, 242–6 (2012). URL <https://www.ncbi.nlm.nih.gov/pubmed/22343383>.
 - ¹⁶ Fölsch, S., Martínez-Blanco, J., Yang, J., Kanisawa, K. & Erwin, S. C. Quantum dots with single-atom precision. *Nature Nanotech* **9**, 505–508 (2014).
 - ¹⁷ Huff, T. *et al.* Binary atomic silicon logic. *Nature Electronics* **2019 2:4** **1**, 636–643 (2018).
 - ¹⁸ He, Y. *et al.* A two-qubit gate between phosphorus donor electrons in silicon. *Nature* **571**, 371–375 (2019). URL <https://doi.org/10.1038/s41586-019-1381-2>.
 - ¹⁹ Yoo, M. J. *et al.* Scanning Single-Electron Transistor Microscopy: Imaging Individual Charges. *Science* **276**, 579–582 (1997).
 - ²⁰ Sellier, H. *et al.* On the imaging of electron transport in semiconductor quantum structures by scanning-gate microscopy: successes and limitations. *Semicond. Sci. Technol.* **26**, 064008 (2011).
 - ²¹ Dombrowski, R., Steinebach, C., Wittneven, C., Morgenstern, M. & Wiesendanger, R. Tip-induced band bending by scanning tunneling spectroscopy of the states of the tip-induced quantum dot on InAs(110). *Phys. Rev. B* **59**, 8043–8048 (1999).
 - ²² Freitag, N. M. *et al.* Electrostatically confined monolayer graphene quantum dots with orbital and valley splittings. *Nano Letters* **16**, 5798–5805 (2016). URL <https://doi.org/10.1021/acs.nanolett.6b02548>.
 - ²³ Salfi, J. *et al.* Valley filtering in spatial maps of coupling between silicon donors and quantum dots. *Physical Review X* **8**, 031049 (2018). URL <https://link.aps.org/doi/10.1103/PhysRevX.8.031049>.
 - ²⁴ Shim, Y.-P., Ruskov, R., Hurst, H. M. & Tahan, C. Induced quantum dot probe for material characterization. *Appl. Phys. Lett.* **114**, 152105 (2019).
 - ²⁵ Wagner, C. *et al.* Quantitative imaging of electric surface potentials with single-atom sensitivity. *Nature Materials* (2019). URL <https://doi.org/10.1038/s41563-019-0382-8>.
 - ²⁶ Malinowski, F. K. *et al.* Fast spin exchange across a multielectron mediator. *Nat Comms* **10**, 1196 (2019).
 - ²⁷ Srinivasa, V., Xu, H. & Taylor, J. M. Tunable Spin-Qubit Coupling Mediated by a Multielectron Quantum Dot. *Phys. Rev. Lett.* **114**, 226803 (2015).
 - ²⁸ Elzerman, J. M. *et al.* Single-shot read-out of an individual electron spin in a quantum dot. *Nature* **430**, 431–435 (2004). URL <http://www.nature.com/doi/10.1038/430431a>.
 - ²⁹ Bonet, E., Deshmukh, M. M. & Ralph, D. C. Solving rate equations for electron tunneling via discrete quantum states. *Physical Review B* **65**, 045317 (2002). URL <https://link.aps.org/doi/10.1103/PhysRevB.65.045317>.
 - ³⁰ Hatem, L. *et al.* Scanning tunneling spectroscopy reveals a silicon dangling bond charge state transition. *New Journal of Physics* **17**, 073023 (2015). URL <http://stacks.iop.org/1367-2630/17/i=7/a=073023>.
 - ³¹ Salfi, J. *et al.* Spatially resolving valley quantum interference of a donor in silicon. *Nat Mater* **13**, 605–10 (2014). URL <https://www.ncbi.nlm.nih.gov/pubmed/24705384>.
 - ³² Taucer, M. *et al.* Single-electron dynamics of an atomic silicon quantum dot on the h-si(100)-(2 x 1) surface. *Physical Review Letters* **112**, 256801 (2014). URL <https://link.aps.org/doi/10.1103/PhysRevLett.112.256801>.
 - ³³ Foxman, E. B. *et al.* Effects of quantum levels on transport through a coulomb island. *Physical Review B* **47**, 10020–10023 (1993). URL <https://link.aps.org/doi/10.1103/PhysRevB.47.10020>.
 - ³⁴ Le, N. H., Fisher, A. J. & Ginossar, E. Extended Hubbard model for mesoscopic transport in donor arrays in silicon. *Phys. Rev. B* **96**, 245406 (2017).
 - ³⁵ Le, N. H., Fisher, A. J., Curson, N. J. & Ginossar, E. Topological phases of a dimerized Fermi-Hubbard model (2019). 1906.00488.